14th International Symposium on Turbulence and Shear Flow Phenomena (TSFP14)
Heidelberg, Germany, July 28–31, 2026

TRANSIENT GROWTH IN UNSTEADY GUST-AIRFOIL ENCOUNTERS

Alec J. Linot
Department of Chemical and Biomolecular Engineering
University of Massachusetts, Amherst
MA 01002, USA
alinot@umass.edu

Kunihiko Taira
Department of Mechanical and Aerospace Engineering
University of California, Los Angeles
CA 90095, USA
ktaira@seas.ucla.edu

ABSTRACT

When small vehicles fly in gusty conditions, they experience massive lift fluctuations and flow separation. Mitigating the effects of these gusts during encounters is important in enabling stable flight in these violent atmospheric environments. In the present study, we seek to improve our understanding of the stability characteristics of flows associated with these extreme gust encounters. Although much is known about the stability of steady and periodic flows, far less is known about the stability of unsteady, aperiodic flows. Due to the time-varying nature of these flows, standard linear stability analysis is insufficient, as it only provides asymptotic stability. Instead, we must consider the *transient growth* of perturbations when analyzing unsteady flows. Here, we study transient growth during extreme gust-airfoil encounters around NACA0012 airfoils.

We perform this analysis by simulating the two-dimensional laminar flow for the gust vortex-airfoil encounter. Taking this flow as the time-varying base state, we seek the three-dimensional optimal perturbations on top of these flows using a spanwise Fourier decomposition. At Reynolds numbers as low as 300, we find that low-wavenumber perturbations to gust-airfoil encounters grow orders of magnitude larger than perturbations to an airfoil or a gust alone. This growth happens through a combination of growth around the gust and around the airfoil that strongly amplifies once the gust impinges on the airfoil, causing vorticity roll-up into a leading-edge vortex above the airfoil surface.

BACKGROUND

Small vehicles fly in a wide variety of environments where unsteadiness is common, such as in the wake of other vehicles, urban canyons, and mountainous terrain. In these types of environments, vehicles can experience gusts whose velocity is comparable to the freestream velocity (Jones, 2020). Flying in these conditions is a major challenge, and many aspects of these flows remain unexplored. Much of the work in understanding gust encounters has involved measuring transient forces and moments on a wing in experiments (Jones *et al.*, 2022) and simulations (Lopez-Doriga *et al.*, 2025) with other works investigating how to actuate to mitigate these forces (Menon & Mittal, 2020; Fukami *et al.*, 2024).

While many studies investigate the aerodynamic forces under a variety of gust conditions and airfoil shapes, few studies consider the stability of these gust-airfoil interactions. A challenge when judging stability is first determining what stability means for a transient gust encounter. Standard linear stability analysis provides the asymptotic behavior of perturbations, making it unsuitable for studying rapidly varying baseflows. Instead, a variety of methods have been introduced to try to understand the stability of unsteady flows (Linot *et al.*, 2025).

One such approach that has been applied to gust-airfoil encounters is the optimally time-dependent (OTD) mode analysis (Zhong *et al.*, 2025). This approach offers insight into the instantaneous directions of greatest growth for a perturbation. Another approach that has been used to study airfoils (He *et al.*, 2019) and gusts (Antkowiak & Brancher, 2004) in isolation is nonmodal stability analysis. In nonmodal stability analysis, the transient growth of perturbations can be studied by finding the *optimal perturbation* (Schmid & Henningson, 2001). The optimal perturbation is the perturbation that grows the largest over some finite time horizon, which makes it ideal for understanding the stability characteristics of unsteady flows. As such, in this work, we investigate the nonmodal stability of gust-airfoil encounters by computing the optimal perturbations to these baseflows under various conditions.

METHODS

Our analysis focuses on the stability of gust-airfoil encounters, which requires a baseflow on top of which we perform the stability analysis. Here, we determine the baseflow by performing direct numerical simulations of Taylor vortices colliding with a NACA0012 airfoil. The Taylor vortex is defined by

$$u_\theta = u_{\theta,\max} \frac{r}{R} \exp\left(\frac{1}{2} - \frac{r^2}{2R^2}\right) \tag{1}$$

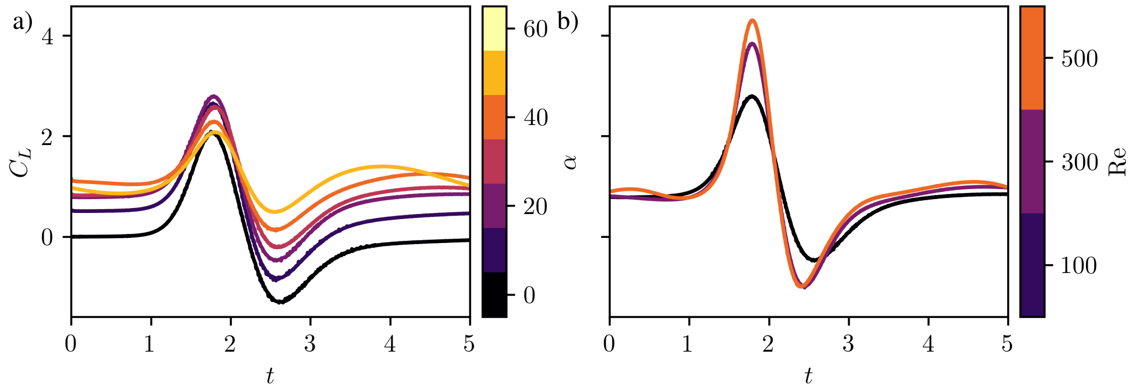

Figure 1: Lift response for gust-airfoil encounters at various a) angles of attack (α) with Re $= 100$ and b) Reynolds numbers (Re) with $\alpha = 20°$.

with a gust ratio $G_r = u_{\theta,\max}/u_\infty = 2$ and Reynolds number Re $= u_\infty c/\nu$. Here, u_θ is the angular velocity, u_∞ is the freestream velocity, r is the radial direction, R is the gust radius, c is the chord length, ν is the kinematic viscosity, and $u_{\theta,\max}$ is the maximum angular velocity. We place the leading edge of the airfoil at the origin, and initialize a Taylor vortex of radius $R = 1/4$ two chord lengths upstream, which convects and collides with the airfoil.

We simulate the gust-airfoil encounter using the immersed boundary projection method (IBPM) (Taira & Colonius, 2007). In the IBPM, we solve the incompressible Navier-Stokes equations (NSE)

$$\frac{\partial \mathbf{u}}{\partial t} + \mathbf{u}\cdot\nabla\mathbf{u} = -\nabla p + \frac{1}{\mathrm{Re}}\nabla^2\mathbf{u} + \int_S \mathbf{f}(\xi(s,t))\delta(\xi - \mathbf{x})ds, \quad (2)$$

and $\nabla\cdot\mathbf{u} = 0$. Here, $\mathbf{u}$ is the velocity, p is the pressure, and $\xi(s,t) \in \partial\mathscr{B}$ are the points on the immersed object $\mathscr{B}$ parameterized by s. These quantities are nondimensionalized using the freestream velocity u_∞ and chord length c. The boundary forcing $\mathbf{f}$ is used to satisfy the no-slip and no-penetration conditions at the boundary $\mathbf{u}(\xi(s,t)) = \int_V \mathbf{u}(\mathbf{x})\delta(\mathbf{x}-\xi)d\mathbf{x} = \mathbf{u}_B(\xi(s,t))$, where $\mathbf{x} \in \mathscr{D}$ lies in the computational domain. We temporally integrate the viscous terms using the implicit Crank–Nicolson (CN) and the convective terms with the explicit second-order Adams-Bashforth.

The gust encounter produces an unsteady baseflow, which requires analysis methods like nonmodal stability (Linot *et al.*, 2024, 2025). To investigate stability characteristics, we decompose the velocity into a baseflow $\mathbf{U}(x,y,t) = [U(x,y,t), V(x,y,t), 0]$ and a perturbation $\mathbf{u}'(x,y,z,t) = [u(x,y,z,t), v(x,y,z,t), w(x,y,z,t)]$, such that $\mathbf{u} = \mathbf{U} + \mathbf{u}'$. Then we linearize the NSE around the baseflow, resulting in $\partial\mathbf{u}'/\partial t = \mathscr{L}(\mathbf{U})\mathbf{u}'$. Due to the spanwise homogeneity in the z-direction, we further simplify this equation by representing the perturbation in terms of Fourier modes $\mathbf{u}'(x,y,z,t) = \int_{-\infty}^{\infty}\hat{\mathbf{u}}(x,y,\beta,t)e^{i\beta z}d\beta$. This allows us to evaluate the linearized equations for each wavenumber separately $\partial\hat{\mathbf{u}}/\partial t = \hat{\mathscr{L}}(\mathbf{U},\beta)\hat{\mathbf{u}}$. The linearized equations of motion can be used to find the fundamental solution operator $A(t,\beta)$, which maps the perturbation $\hat{\mathbf{u}}$ forward in time $\hat{\mathbf{u}}(t,\beta) = A(t,\beta)\hat{\mathbf{u}}(0,\beta)$. This operator can be explicitly computed using the product of matrix exponentials $A(t,\beta) = \Pi_{j=1}^{N}\exp\left[\mathscr{L}(\mathbf{U}(t_j),\beta)\Delta t\right]$.

With the fundamental solution operator, we determine the maximum possible amplification as

$$G(t;\beta) = \max_{\hat{\mathbf{u}}(0)\neq 0}\frac{||\hat{\mathbf{u}}(t)||_E^2}{||\hat{\mathbf{u}}(0)||_E^2} = \max_{\hat{\mathbf{u}}(0)\neq 0}\frac{||A(t)\hat{\mathbf{u}}(0)||_E^2}{||\hat{\mathbf{u}}(0)||_E^2}, \quad (3)$$

where $\|\cdot\|_E$ denotes the energy norm. This amplification is the largest growth of any unit norm perturbation propagated forward to time t. The perturbation that causes this growth is the optimal perturbation. These quantities come from the singular value decomposition (SVD) of $A(t)$ – with appropriate weighting for the energy norm. The squared principal singular value squared (σ_1^2) gives the maximum gain $G(t)$, and the associated optimal perturbation is the right principal singular vector.

The fundamental solution operator can be computed by discretizing the linearized equations of motion into a matrix form. Unfortunately, this matrix scales with the number of grid points squared, making the SVD of $A(t)$ infeasible in many cases. By observing that the squared leading singular value of $A(t)$ equals the leading eigenvalue of $A^*(t)A(t)$, we can overcome the challenge. The leading eigenvalue of $A^*(t)A(t)$ can be computed without forming $A(t)$ or $A^*(t)$ through power iterations. Initial conditions are evolved forward with the linearized equations giving $\hat{\mathbf{u}}(t) = A(t)\hat{\mathbf{u}}(0)$, then the adjoint equations are evolved backward, giving $\hat{\mathbf{u}}(0) = A^*(t)\hat{\mathbf{u}}(t)$, which we then normalize. Iterating this procedure results in the initial perturbation converging to the optimal perturbation. For a discussion on how to construct the linear and adjoint equations, refer to (Barkley *et al.*, 2008).

RESULTS

Using the above methods, we performed a sweep of optimal perturbation calculations for Re $= \{100, 300, 500\}$, $\alpha = \{0°, 10°, 20°, 30°, 40°, 50°\}$, $\beta = \{0, \pi/2, \pi, 2\pi\}$, and $t_{\text{opt}} = \{1,2,3,4,5\}$. All simulations were performed in a domain of $x \in [-8, 24]$ and $y \in [-15, 15]$ on a staggered Cartesian grid of size $[N_x, N_y] = [640, 320]$ with a timestep $\Delta t = 2.5 \times 10^{-3}$. The baseflow uses Dirichlet boundary conditions on the left, top, and bottom sides and the convective outflow boundary condition on the right side ($\partial\mathbf{U}/\partial t + u_\infty\partial\mathbf{U}/\partial x = 0$). We run all simulations to the steady-state or periodic dynamics before introducing the gust. We do not observe a strong dependency on the gust timing in the periodic cases for the parameter regimes considered here. Figure 1 shows how the evolution of the lift coefficient changes for these simulations. The gust induces a large increase in lift, followed by a drop in lift before stabilizing at around 5 convective times. We focus on the growth of optimal perturbations in this time range because the gust plays a small role in the lift on the airfoil past this point.

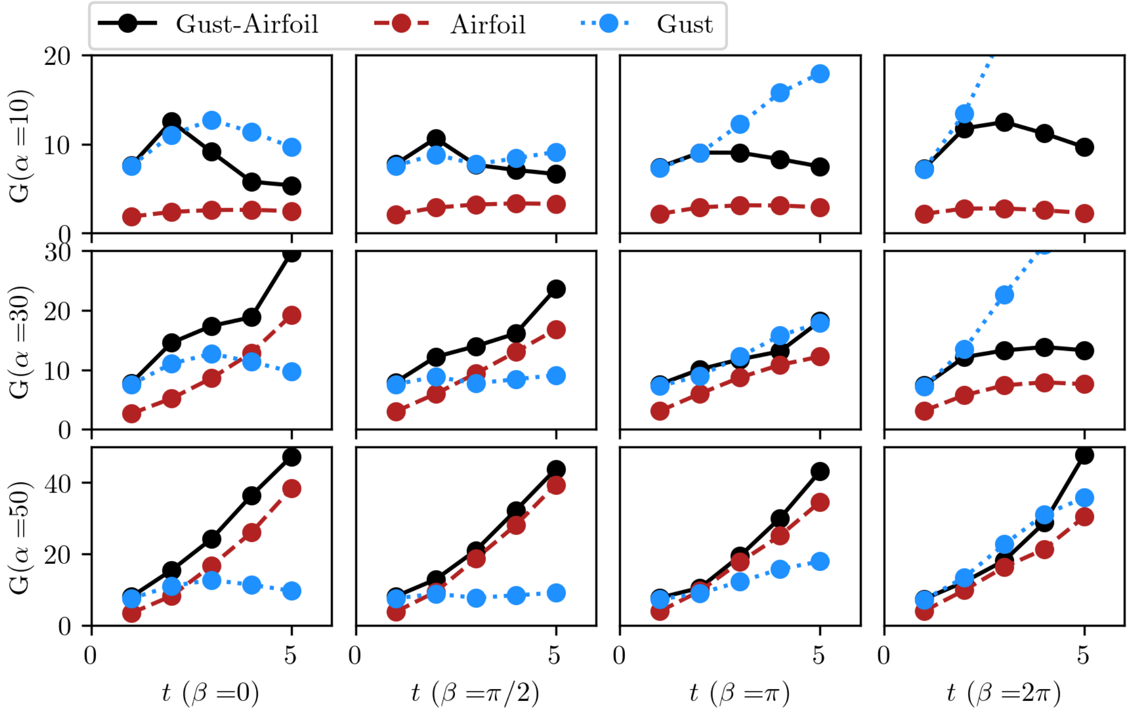

Figure 2: Transient growth of perturbations to gust-airfoil encounters, airfoils, and gusts alone. The angle of attack and the spanwise wavenumber of the perturbation are varied. The Reynolds number is fixed at $\mathrm{Re} = 100$.

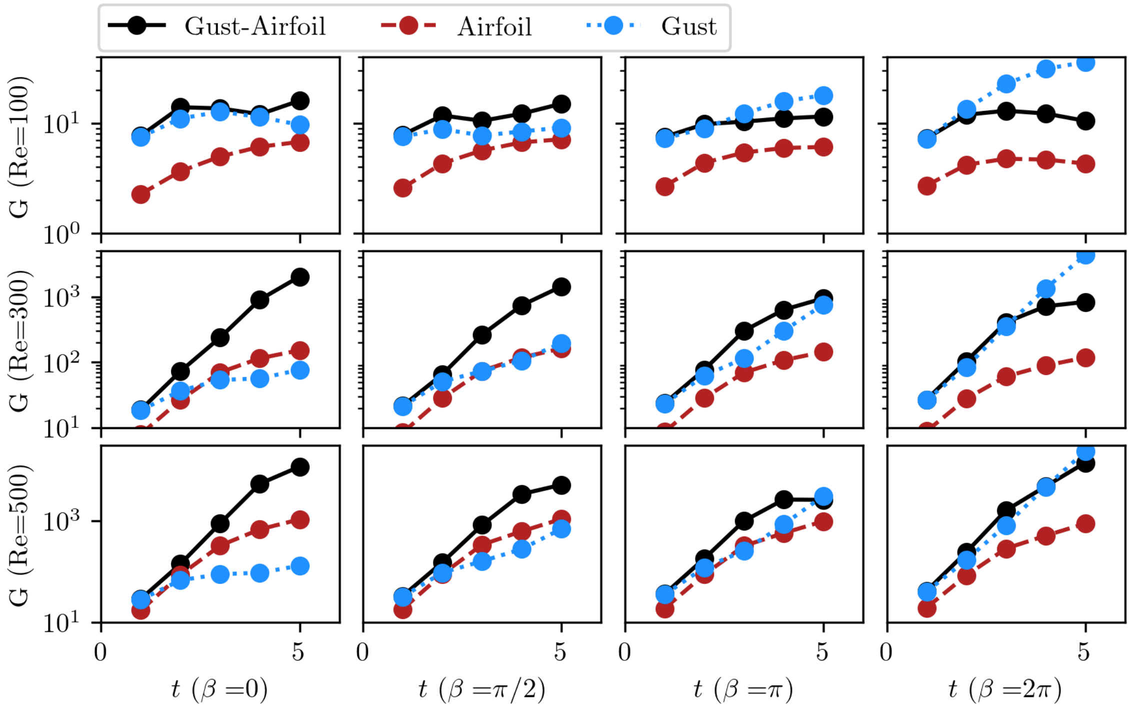

Figure 3: Transient growth of perturbations to gust-airfoil encounters, airfoils, and gusts alone. The Reynolds number and the spanwise wavenumber of the perturbation are varied. The angle of attack is fixed at $\alpha = 20°$.

Optimal Perturbations

With these baseflows, we computed optimal perturbations using the linear and adjoint equations – both with zero Dirichlet boundary conditions. The perturbations never approach the boundaries, so this choice does not influence the results. We iterated until the relative error in the optimal perturbation dropped below 1%. For each trial, we consider the maximum amplification for the gust-airfoil encounter, for the airfoil without the gust, and for the gust without the airfoil. Considering these three cases allows us to determine if the gust encounter introduces new perturbation dynamics, or if the perturbation dynamics are a combination of the gust or airfoil in isolation.

First, we investigate varying the angle of attack at a low Reynolds number ($\mathrm{Re} = 100$). Figure 2 shows the maximum amplification as we vary β for the different angles of attack. At early times (∼1-2 convective times), the growth in the gust-airfoil encounter agrees with the growth in the gust alone. This happens because the gust has not interacted with the airfoil yet. Thus, when comparing these three cases, we will predominantly focus on what happens at later times.

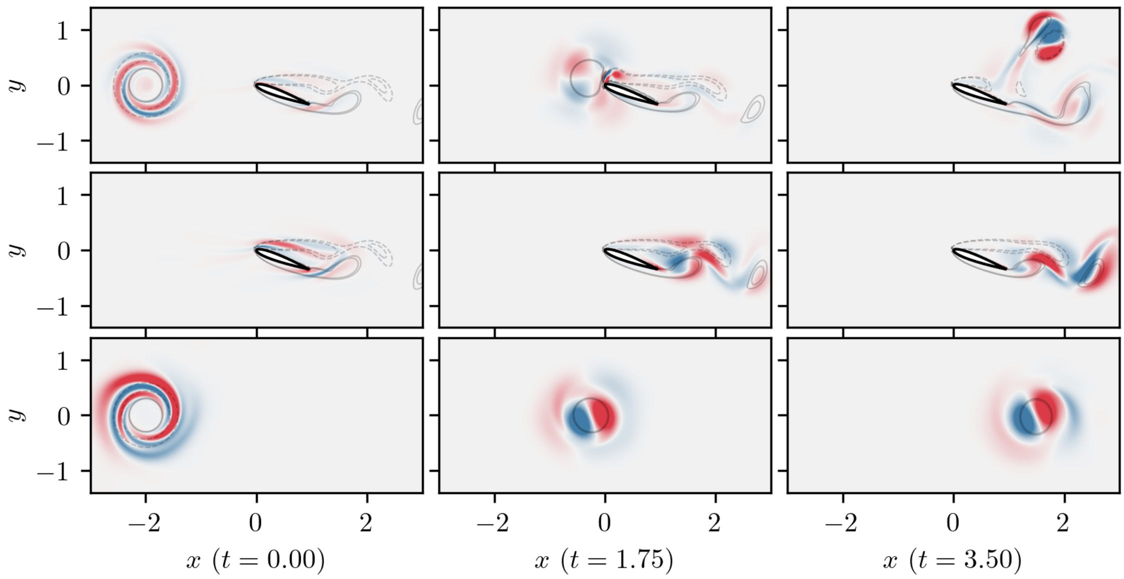

Figure 4: Compares perturbation evolution for gust-airfoil encounters, airfoils, and gusts alone. Vorticity of the baseflow is shown with contours (positive solid, negative dashed), and of the perturbation is shown with color (positive red, negative blue). The perturbation vorticity is scaled by the max value at each time.

For $\alpha = 10^\circ$, the maximum amplification of the gust-airfoil encounter behaves more like the gust alone, with the airfoil always showing much lower maximum amplification. However, when β becomes sufficiently large, the maximum amplification of the gust-airfoil encounter falls behind that of the gust alone. For $\alpha > 10^\circ$, the maximum amplification of the airfoil starts to increase. This causes the maximum amplification in the gust-airfoil encounter to typically behave more like the gust alone at early times, and the airfoil alone at later times. This suggests, at this Reynolds number, that studying the gust or airfoil alone may be sufficient to understand the gust-airfoil encounter; however, this is not true as we increase the Reynolds number.

Next, we investigate varying the Reynolds number at a fixed angle of attack ($\alpha = 20^\circ$. Figure 3 shows the maximum amplification as we vary β for the different Reynolds numbers. At Re $= 300$ and Re $= 500$, all cases become less stable. In particular, perturbation energy dramatically amplifies for the gust-airfoil encounter at low values of β. This growth is orders of magnitude greater than the other two cases, indicating that the baseflow must be amplifying growth through some mechanism that only appears during the gust-airfoil encounter. As β increases, the maximum amplification for the gust increases and becomes larger or comparable to the maximum amplification for the gust-airfoil encounter at $\beta = 2\pi$. Due to the apparent unique physics happening at low values of β in the gust-airfoil encounter case, we will focus on this regime.

Growth Mechanism

Finally, we investigate the growth mechanism in the gust-airfoil encounter at $[\mathrm{Re}, \alpha, \beta] = [300, 20^\circ, 0]$. Figure 4 shows the evolution of the optimal perturbations computed at $t_{\mathrm{opt}} = 4$ in the three cases. The initial condition in the gust-airfoil encounter forms a spiral around the gust and stripes of vorticity around the airfoil, which largely resembles a combination of the optimal perturbations in the two other cases. Upon colliding with the airfoil, the gust causes the vorticity of the baseflow to roll up into a leading-edge vortex. At the vortex roll-up location, we see strong perturbation vorticity. Finally, a vortex dipole forms and is pushed away from the surface. The perturbation then grows by extracting large amounts of energy in the high-shear region between these vortex dipoles. The gust-only and airfoil-only cases never generate a vortex dipole; thus, they never experience the growth mechanism observed in the gust-airfoil encounter. At low values of β this growth is an order of magnitude larger than the other cases.

This growth can be better understood by examining the perturbation energy $E = 1/2 \int_V \mathbf{u}' \cdot \mathbf{u}' dV$. The time evolution of the perturbation energy is given by the energy equation (Serrin, 1959; Conrad & Criminale, 1965)

$$\frac{dE}{dt} = \underbrace{-\int_V \frac{1}{\mathrm{Re}} \nabla \mathbf{u}' : \nabla \mathbf{u}' \, dV}_{\text{dissipation (D)}} \underbrace{- \int_V \mathbf{u}' \cdot \nabla \mathbf{U} \cdot \mathbf{u}' \, dV}_{\text{production (P)}} . \tag{4}$$

This equation allows us to isolate the effects of dissipation and production, and the integrand of each of these terms can highlight how the perturbation and the baseflow interact. Figure 5 shows how the energy production varies through time. The gust-encounter exhibits two peaks of production, while the other airfoil and gust alone only show one initial peak in production that decays over time. To explain what causes this difference, we show the time evolution of the production integrand in Figure 6. For the airfoil, the perturbations convect away from the body, which causes this decay. For the gust, the perturbations form a dipole that rotates with the gust. In both these cases, the shape of the perturbation relative to the baseflow does not change substantially at long times, but the magnitude of the baseflow decreases, causing the production to drop.

Perturbations to the gust-airfoil encounter show much larger growth, which is reflected in the production curve. For the gust-airfoil encounter, there is a high initial peak in the production, followed by a large drop, and then a second peak. Figure 6 shows the integrand of production at these three times. At early times, energy is produced in spirals around the gust. Notably, the perturbation differs from the perturbation to the gust alone. This indicates that the perturbation to the gust-airfoil encounter identifies a perturbation that causes greater short-time growth, but would decay faster if it were applied to the gust alone.

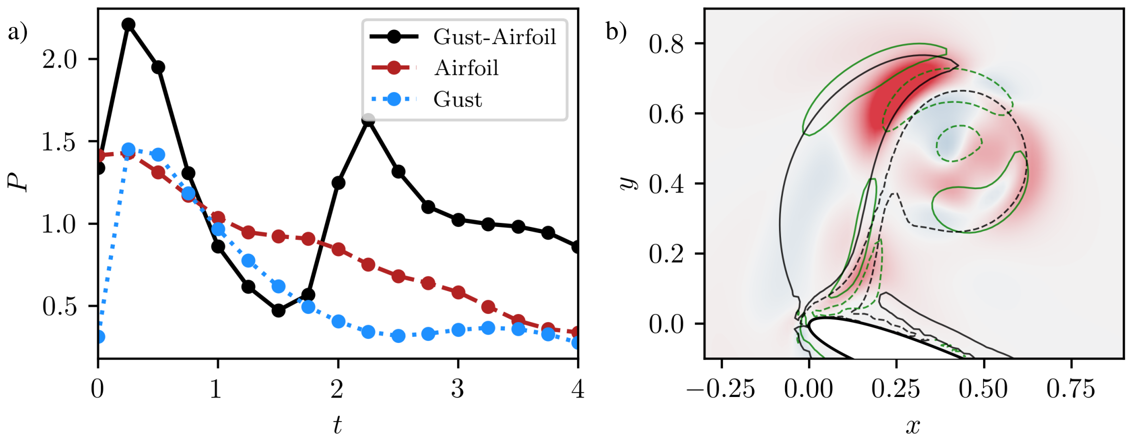

Figure 5: a) Perturbation energy production over time for gust-airfoil encounters, airfoils, and gusts alone. b) Zoom in on the spatial production at $t = 2.25$ for the gust-airfoil encounter. Black contours show baseflow vorticity (solid positive, dashed negative), green contours show perturbation vorticity (solid positive, dashed negative), and colors show the spatial production (red positive, blue negative).

At the minimum of production, the gust is beginning the collision with the airfoil. At this point in time, the production begins to increase again as energy starts to be added to the perturbation due to the roll-up of the leading-edge vortex. Finally, we see at the second peak that the perturbation interacts with the baseflow vortex dipole, leading to large energy production. Figure 5 zooms in on the production that occurs as the baseflow vortex dipole forms. The interaction between the baseflow and the perturbation leads to the greatest production inside of the two baseflow vortices that make up the dipole. After the second production peak, the energy production decreases, but not as rapidly as in the other two scenarios. The long periods of high production in the gust-airfoil encounter are what cause the energy of this perturbation to grow much larger than in the other two scenarios.

Lift Modifications in DNS

Now that we have the optimal perturbations identified, we can examine the effect of these perturbations when applied to the DNS. Figure 7 shows the lift response as we add and subtract the optimal perturbation ($\beta = 0$, $t_{\text{opt}} = 4$) for the gust-airfoil encounter at $\text{Re} = 300$, $\alpha = 20°$. As the sign of the optimal perturbation is arbitrary, we investigate both the effect of adding and subtracting the optimal perturbation. Adding the optimal perturbation results in a small drop in the unperturbed gust that would have collided with the airfoil. Following this dip, the lift peak is reduced. However, the drop in lift does not change substantially. This suggests that adding the perturbation in this fashion reduces the size of the initial interaction, but still causes vortex dipoles to form from rollup on the leading edge. While not shown in this paper, this is evident from the time series.

Changing the sign of the optimal perturbation leads to a more dramatic change in the lift response. When subtracting the optimal perturbation, we see a reduction in the amplitude of both the minimum and maximum values of lift. As the magnitude of the perturbation increases, the lift minimum is reduced first, followed by the lift maximum. The minimum is eliminated because the perturbation interacts with the baseflow in such a way that the vortex dipole never forms off the leading edge. When the perturbation magnitude becomes sufficiently large, the vortex breaks apart before interacting with the airfoil.

These results indicate that it may be possible to use non-modal stability analysis to identify forcing profiles to eliminate lift fluctuations during gust encounters, or to identify mechanisms to break gusts apart before interacting with other objects downstream. In this case, the control is not realizable because much of the optimal perturbation lies in the gust. This shortcoming can be remedied by windowing the optimal perturbations to specific regions of the flow where control is possible.

CONCLUSION

In this study, we explored the stability of positive Taylor vortices interacting with NACA0012 airfoils. We found that, when the Reynolds number is low, the stability of the gust-airfoil encounter is similar to that of the gust alone at low angles of attack, and similar to that of the airfoil alone at high angles of attack. The exception to this is at high spanwise wavenumbers and low angles of attack, where perturbations to the gust alone grow much larger than to the gust-airfoil encounter.

When the Reynolds number is high, we observed a unique regime at low spanwise wavenumber, where perturbations to the gust-airfoil interaction experienced orders of magnitude greater growth than to the gust or airfoil alone. We focused on this regime to better understand the mechanism responsible for inducing this growth. In this regime, we found that perturbations were able to grow much larger because there were two phases of growth. First, the perturbation grew with spirals around the gust, and then there was a second peak in energy production during vortex roll-up of the baseflow. This indicates that the gust-airfoil encounter could, over short times, take advantage of faster-growing perturbations that would decay away in the gust-only case. Then, a second period of growth occurred that allowed this perturbation to grow larger in the high-shear region during vortex roll-up. This mechanism explains why there is an order of magnitude greater growth in the gust-airfoil encounter. Finally, we put this optimal perturbation back into the nonlinear simulation. At sufficiently high amplitudes, the optimal perturbation effectively eliminated all lift fluctuations.

REFERENCES

Antkowiak, Arnaud & Brancher, Pierre 2004 Transient energy growth for the Lamb–Oseen vortex. *Physics of Fluids* **16** (1), L1–L4.

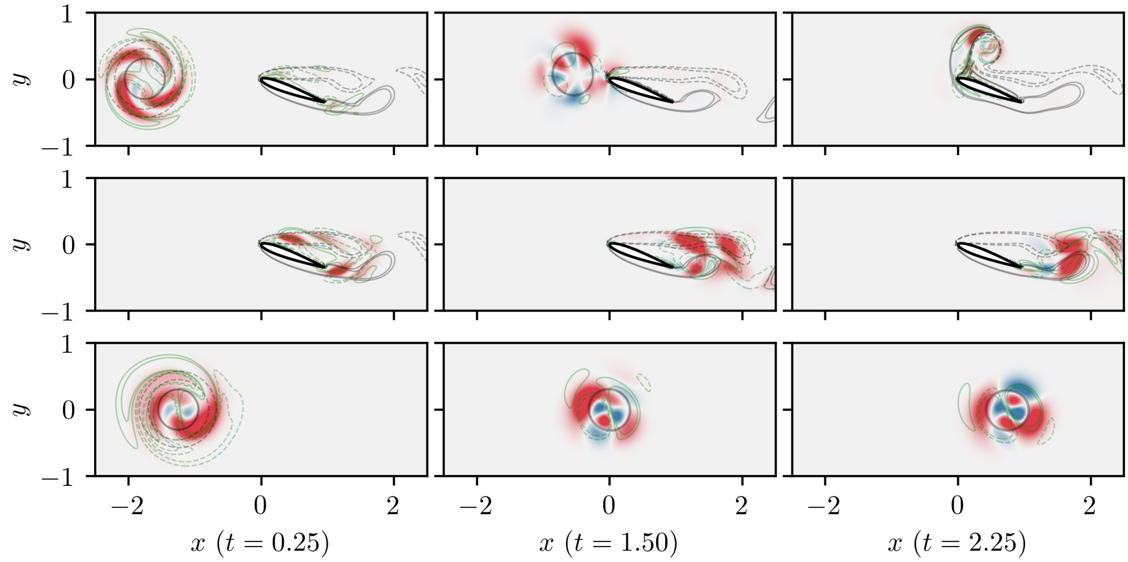

Figure 6: Compares spatial production evolution for gust-airfoil encounters, airfoils, and gusts alone. Black contours show baseflow vorticity (solid positive, dashed negative), green contours show perturbation vorticity (solid positive, dashed negative), and colors show the spatial production (red positive, blue negative). The spatial production is scaled by the max value at each time.

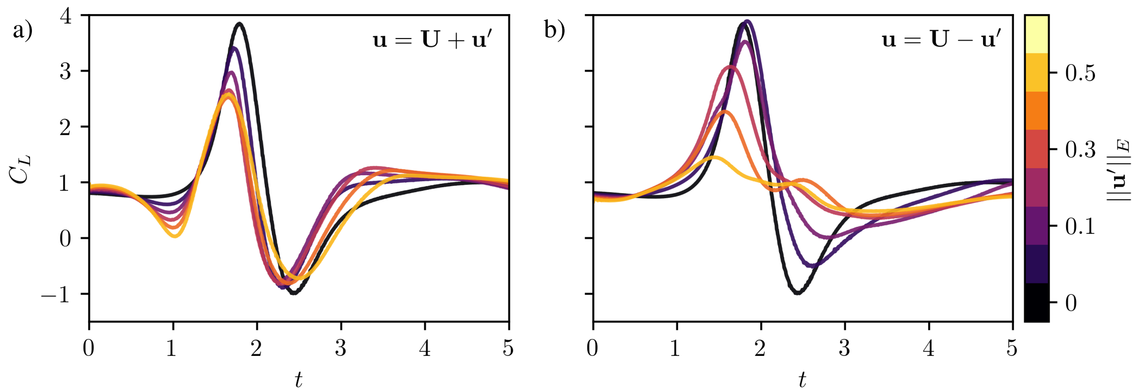

Figure 7: Lift response for gust-airfoil encounters at Re $= 300$, $\alpha = 20°$ as the optimal perturbation at $\beta = 0$, $t_{\text{opt}} = 4$ is added to the nonlinear simulation. a) shows adding the optimal perturbation, and b) shows subtracting the optimal perturbation.

Barkley, D., Blackburn, H. M. & Sherwin, S. J. 2008 Direct optimal growth analysis for timesteppers. *International Journal for Numerical Methods in Fluids* **57** (9), 1435–1458.

Conrad, Peter W. & Criminale, William O. 1965 The stability of time-dependent laminar flow: Parallel flows. *Z. Angew. Math. Phys.* **16** (2), 233–254.

Fukami, Kai, Nakao, Hiroya & Taira, Kunihiko 2024 Data-driven transient lift attenuation for extreme vortex gust–airfoil interactions. *Journal of Fluid Mechanics* **992**, A17.

He, Wei, Pérez, José Miguel, Yu, Peng & Li, Larry K.B. 2019 Non-modal stability analysis of low-re separated flow around a NACA 4415 airfoil in ground effect. *Aerospace Science and Technology* **92**, 269–279.

Jones, Anya R. 2020 Gust encounters of rigid wings: Taming the parameter space. *Phys. Rev. Fluids* **5**, 110513.

Jones, Anya R., Cetiner, Oksan & Smith, Marilyn J. 2022 Physics and modeling of large flow disturbances: Discrete gust encounters for modern air vehicles. *Annual Review of Fluid Mechanics* **54** (Volume 54, 2022), 469–493.

Linot, Alec J, Lopez-Doriga, Barbara, Zhong, Yonghong & Taira, Kunihiko 2025 Extracting dominant dynamics about unsteady base flows. *Fluid Dynamics Research* **57** (3), 031401.

Linot, Alec J., Schmid, Peter J. & Taira, Kunihiko 2024 On the laminar solutions and stability of accelerating and decelerating channel flows. *Journal of Fluid Mechanics* **999**, A43.

Lopez-Doriga, Barbara, Jones, Anya R. M. & Taira, Kunihiko 2025 On the effect of airfoil geometry on extreme vortex-gust encounters. *ArXiv 2510.15154* .

Menon, Karthik & Mittal, Rajat 2020 Aeroelastic response of an airfoil to gusts: Prediction and control strategies from computed energy maps. *Journal of Fluids and Structures* **97**, 103078.

Schmid, Peter J. & Henningson, Dan S. 2001 *Stability and Transition in Shear Flows*, *Applied Mathematical Sciences*, vol. 142. New York, NY: Springer New York.

Serrin, James 1959 On the stability of viscous fluid motions. *Archive for Rational Mechanics and Analysis* **3** (1), 1–13.

Taira, Kunihiko & Colonius, Tim 2007 The immersed boundary method: A projection approach. *Journal of Computational Physics* **225** (2), 2118–2137.

Zhong, Yonghong, Amiri-Margavi, Alireza, Babaee, Hessam & Taira, Kunihiko 2025 Optimally time-dependent modes of vortex gust–airfoil interactions. *Journal of Fluid Mechanics* **1006**, A18.